Journal of Engineering Mathematics **29:** 393–412, 1995.

Application of the boundary integral method to the interaction of rising two-dimensional deformable gas bubbles

P.B. ROBINSON[1], J.M. BOULTON-STONE[2] and J.R. BLAKE[2]
[1]*DRA Fort Halstead, Sevenoaks, Kent TN14 7BP, United Kingdom*
[2]*School of Mathematics and Statistics, The University of Birmingham, Edgbaston, Birmingham B15 2TT, United Kingdom*

Received 27 April 1993; accepted in revised form 28 October 1994

Abstract. The boundary integral method is applied to model the initial motion of two-dimensional or cylindrical deformable gas bubbles in an inviscid, incompressible fluid. Following the success of recent boundary integral studies to predict the qualitative behaviour of a single gas bubble, this numerical study is extended to consider the interaction of several bubbles. Surface tension, relative initial position and volume are all found to be important factors affecting the bubble interaction, jet formation, "trapping" of fluid between bubbles and bubble shedding. As well as computing the evolution of the bubble surfaces, consideration of the pressure fields and resulting instantaneous streamlines is given.

1. Introduction

The behaviour of a single two-dimensional deformable gas bubble rising in a fluid under gravity, has been studied by several investigators using both experimental and numerical techniques. Walters and Davidson [1] investigated the motion of a large circular bubble, initially at rest in a stagnant fluid. As predicted by irrotational flow theory, the initial acceleration following release is that of gravity. Their theory also predicts that a liquid jet should be projected up from the base of the bubble into its interior. These predictions were confirmed by experiment, where a gas bubble of initial radius 1 in. was released in a column of water contained between two vertical perspex sheets 3/8 in. apart. High-speed photography revealed that as the bubble distorts, the liquid jet tip never penetrates the top surface of the interface, but rather slows and broadens forming a horseshoe shape bubble. This distortion ultimately causes bubble break-up into a cylindrical-cap bubble with two small bubbles detached at its rear.

As suggested by Walters and Davidson, an expansion of the solution in powers of t was made by Baumel *et al.* [2]. They successfully followed the motion of the two points lying on the bubble's vertical axis of symmetry, by summing the series using Padé approximants. This method did not lead to satisfactory results for values of time greater than about two in dimensionless units, due to a small radius of convergence caused by a pole in the complex t-plane.

More recently, the numerical boundary integral techniques employed by Baker and Moore [3], proved successful in enabling the two-dimensional bubble motion and shape to be followed for larger times until the occurrence of break-up in the manner observed by Walters and Davidson. Comparison between theory and experiment showed the computed jet speed to be greater than that observed experimentally, resulting in the portion of fluid which traverses the bubble to be more slender and slightly longer. Baker and Moore also found that the effect

of surface tension did not remove this discrepancy but suggested that the effects due to the presence of a meniscus or a thin film separating the bubble from the glass may be important. The surface vortex and dipole methods used by Baker and Moore, involve calculating the strengths of either vortices or dipoles respectively distributed along the bubble surface and then estimating the spatial derivatives in terms of cubic splines. The boundary integral method has also been used to model multi-bubble interactions for the case of two cavitation bubbles collapsing near a rigid boundary by Blake *et al.* [4]. However the calculations in [4] assume an axisymmetric geometry. Here, using two dimensions to study the interactions of rising gas bubbles, we are able to break free from such geometric constraints without the complexities of developing an accurate three-dimensional code. Indeed, in the calculations made by Unverdi and Tryggvason [5] of rising two-dimensional gas bubbles in viscous liquids at various Eötvös and Morton numbers, surprising agreement with experiment [6, 7] is found indicating that insight into fully three-dimensional flows can often be gained by examining the somewhat simpler two-dimensional analogue.

The interaction of a pair of rising gas bubbles has been studied on a number of occasions in the past. Theoretical investigations into the relative and centroid motions of two bubbles by Kok [8] has shown good agreement with experiments performed by the same author [9]. The calculation reported in [8], based on potential theory, incorporates viscous drag terms allowing for a correction due to a small deviation from spherical. However Kok points out that the slight disagreement found could be due to some further effect that bubble deformation has on the flow field.

Further detailed study, in relation to bubble coalescence, both of an experimental (Duineveld [10]) and theoretical (Kumaran and Koch [11]) nature has also been undertaken. The theoretical calculations of Kumaran and Koch [11] and van Wijngaarden [12] have also concentrated on low Weber numbers and thus essentially low deformation situations.

By taking a numerical approach in this study, we allow ourselves an opportunity to examine the effect of deformation on the interaction of bubbles at large Weber numbers. The numerical calculations do not include a drag term and so cannot give good comparison with experiment for large times. However they can provide information as to the effect that the deformation has on the interaction.

We also point out that as the bubble size increases, so does the Reynolds number with the consequence of rotational wake formation at moderately large values. The assumption of potential flow can therefore give reasonably accurate information on bubble interaction only when wake formation behind bubbles is small, or when the angle between bubbles is close to 90° (see Duineveld [10]).

The motion of bubbles at high Reynolds numbers contrasts greatly with that of viscous drops at low Reynolds numbers. This can be seen clearly in the calculations and experiments of Manga and Stone [13]. Nevertheless there is a superficial similarity in the bubble trajectories in certain cases, particularly when deformation is small, although the flow reversibility property of Stokes flow ensures an almost symmetric relative approach and retreat of the second drop with respect to the first for low Reynolds numbers.

In the present study, a two dimensional boundary integral method based on Green's formulation of the problem is presented with the addition of several computation examples which illustrate the resulting dynamical behaviour (both centroid motion and deformation) for various combinations of initial bubble size and location. Although the results obtained show a qualitative agreement with that observed previously for a single bubble, long term bubble motions, in particular the relative volume of any detached bubbles, is found to depend

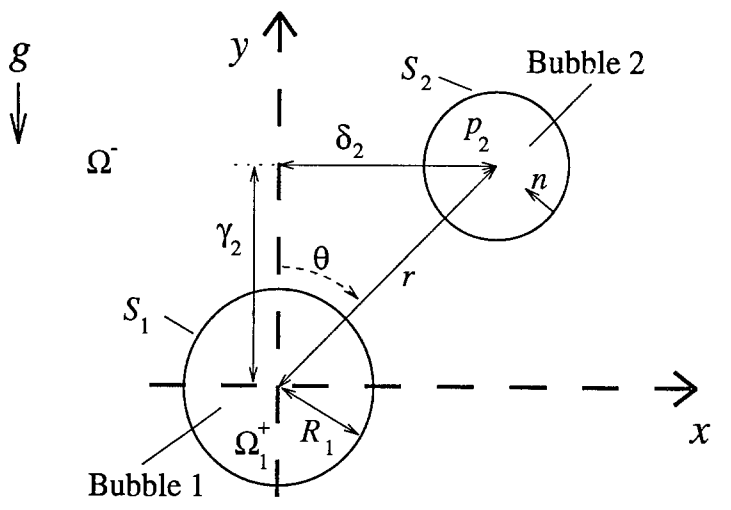

Fig. 1. A schematic illustration showing the initial configuration for systems of two-dimensional bubbles used in the calculations.

sensitively upon the nature of both the mutual bubble interaction and the relative importance of surface tension effects. In order to allow comparison with Baker and Moore's calculations, where there is no net flow from the bubble, we assume here that bubbles remain of constant cross-sectional area.

2. Theory

In keeping with previous theoretical work, motion is assumed two-dimensional and irrotational. The fluid surrounding the bubbles is also assumed infinite, incompressible, irrotational and inviscid, leading to the velocity **u** being expressed as the gradient of a potential φ, *i.e.*

$$\mathbf{u} = \nabla\varphi, \tag{1}$$

with φ satisfying Laplace's equation in the fluid;

$$\nabla^2\varphi = 0. \tag{2}$$

To define the geometry of the problem (see Fig. 1), we let Ω^- be the infinite, multiply connected region representing the surrounding fluid. The N bubble surfaces which form internal boundaries in Ω^- will be represented by simple, piecewise smooth, non-intersecting contours $S_1, S_2, \ldots, S_N$ the union of which will be denoted by S. The union of the finite regions $\Omega_1^+, \ldots \Omega_N^+$, contained in the closed contours $S_1, \ldots, S_N$ respectively, will be denoted by Ω^+.

Fluid particles initially on the bubble surfaces remain there, yielding the kinematic condition

$$\frac{\mathrm{d}\mathbf{x}}{\mathrm{d}t} = \nabla\varphi, \quad \mathbf{x} \in S. \tag{3}$$

The Bernoulli equation which provides the necessary dynamic boundary condition on the bubble surfaces is given by

$$p = p_\infty - \frac{1}{2}\rho|\mathbf{u}|^2 - \rho\frac{\partial\varphi}{\partial t} - \rho g y, \tag{4}$$

where p is the fluid pressure at the bubble boundary, p_∞ the ambient fluid pressure and g the acceleration due to gravity in the $-y$ direction.

We assume that the contents of each bubble behaves as a perfect gas with energy added internally being instantaneously conducted out of the bubble. For such isothermal motion, the internal bubble pressure p_i for each bubble ($i = 1, \ldots, N$) at time t is related to its internal area V_i by

$$p_i(t) = p_i(0)\frac{V_i(0)}{V_i(t)}. \tag{5}$$

If the distance h that a bubble rises is assumed small, such that the change in hydrostatic pressure is small compared to the ambient fluid pressure, then the bubble area, given approximately by

$$V_i(t) = V_i(0)\left(1 - \frac{\rho g h}{p_\infty}\right)^{-1}, \tag{6}$$

can be taken as constant. This assumption is consistent with the single bubble experiments of Walters and Davidson [1] who also noted that the bubble volume remains approximately constant during its evolution.

In the presence of surface tension forces, there exists a discontinuity in pressure across the bubble interface with the increase of internal bubble pressure given by

$$p_i = p + \sigma\kappa, \tag{7}$$

where κ is the curvature of the surface and σ is the surface tension of the interface. If the bubbles are assumed initially circular of radii R_i, as shown schematically in Fig. 1, the initial internal bubble pressures as defined by equations (4) and (7) are given by

$$p_i(0) = p_\infty + \frac{\sigma}{R_i} - pg\gamma_i. \tag{8}$$

Here γ_i is the initial vertical displacement of the bubble i centroid from some reference height which, in Fig. 1, is taken as the height of bubble 1. Correspondingly, δ_i is the initial horizontal displacement. For two bubble-systems, we shall also have occasion to describe the initial position of the centroid of the second bubble, relative to the first, in terms of polar co-ordinates, (r, θ).

Equation (4) can now be written

$$\frac{1}{2}|\mathbf{u}|^2 + \rho\frac{\partial\varphi}{\partial t} + \sigma\left(\frac{1}{R_i} - \kappa\right) + \rho g(y - \gamma_i) + \Delta p_i = 0, \tag{9}$$

where

$$\Delta p_i(t) = p_i(t) - p_i(0). \tag{10}$$

We now introduce the appropriate dimensionless quantities:

$$\bar{x} = \frac{x}{R}, \quad \bar{y} = \frac{y}{R}, \quad \bar{R}_i = \frac{R_i}{R},$$

$$\bar{\gamma}_i = \frac{\gamma_i}{R}, \quad \bar{\delta}_i = \frac{\delta_i}{R}, \quad \bar{r} = \frac{r}{R}, \quad \bar{\kappa} = \kappa R \tag{11}$$

$$\bar{t} = t\left(\frac{g}{R}\right)^{1/2}, \quad \bar{\varphi} = \varphi\left(\frac{1}{gR^3}\right)^{1/2}, \quad \bar{\mathbf{u}} = \mathbf{u}\left(\frac{1}{gR}\right)^{1/2}, \quad \Delta\bar{p}_i = \frac{\Delta p_i}{\rho g R},$$

where R_i is the equivalent bubble radius defined in terms of the internal bubble area by

$$R_i = \left(\frac{V_i}{\pi}\right)^{1/2}, \tag{12}$$

with R the maximum equivalent bubble radius defined by,

$$R = \max_i\{R_i\}, \quad \bar{R} = 1. \tag{13}$$

On dropping bars, equation (9) may be put into the non-dimensional form

$$\frac{D\varphi}{Dt} = \frac{1}{2}|\mathbf{u}|^2 + \frac{4}{\mathrm{Eo}}\left(\kappa - \frac{1}{R_i}\right) + (\gamma_i - y) - \Delta p_i, \tag{14}$$

where Eo the Eötvös number (see for example Harper [14]), is defined by

$$\mathrm{Eo} = \frac{4\rho g R^2}{\sigma}. \tag{15}$$

By introducing a sphere Σ_r of radius r in Ω^- which bounds externally a finite volume V^- between itself and S, Green's formula in the plane can be written,

$$\int_{V^-}(G(\mathbf{x},\mathbf{x}')\nabla^2\varphi(\mathbf{x}') - \varphi(\mathbf{x}')\nabla^2 G(\mathbf{x},\mathbf{x}'))\,\mathrm{d}V' = \int_{S\cup\sum_r}\left(G(\mathbf{x},\mathbf{x}')\frac{\partial\varphi(\mathbf{x}')}{\partial n} - \varphi(\mathbf{x}')\frac{\partial G(\mathbf{x},\mathbf{x}')}{\partial n'}\right)\mathrm{d}S', \tag{16}$$

where G, the two-dimensional Green's function for equation (1) is given by

$$G(\mathbf{x},\mathbf{x}') = \frac{1}{2\pi}\log\frac{1}{|\mathbf{x}-\mathbf{x}'|}. \tag{17}$$

On taking the limit $r \to \infty$ the region V^- tends to Ω^- and the integral over Σ_r yields a constant k (Batchelor [15]), independent of $\mathbf{x}$. Thus for an unbounded fluid the boundary integral becomes

$$c(\mathbf{x})\varphi(\mathbf{x}) = k + \int_S\left(G(\mathbf{x},\mathbf{x}')\frac{\partial\varphi(\mathbf{x}')}{\partial n} - \varphi(\mathbf{x}')\frac{\partial G(\mathbf{x},\mathbf{x}')}{\partial n'}\right)\mathrm{d}S', \tag{18}$$

where

$$c(\mathbf{x}) = \begin{cases} 0, & \mathbf{x}\in\Omega^+, \\ 1, & \mathbf{x}\in\Omega^-, \\ \frac{1}{2} & \mathbf{x}\in S. \end{cases}$$

Upon performing a Taylor expansion of equation (18), the behaviour of $\varphi(\mathbf{x})$ in the far field can be written as,

$$\varphi(\mathbf{x}) = k + \frac{1}{2\pi}\left\{m\log\frac{1}{|\mathbf{x}|} + \boldsymbol{d}\cdot\frac{\mathbf{x}}{|\mathbf{x}|^2}\right\} + O(|\mathbf{x}|^{-2}). \tag{19}$$

On assuming the far-field condition $\varphi(\mathbf{x}) \to 0$ as $|\mathbf{x}| \to \infty$ we see that k may be taken as zero. Clearly the first term on the R.H.S of equation (19) represents source-like behaviour and is proportional to the rate of expansion of Ω^+ with source strength given by,

$$m(t) = \frac{\mathrm{d}V}{\mathrm{d}t} = -\int_S \frac{\partial \varphi}{\partial n}\,\mathrm{d}S, \tag{20}$$

where

$$V = \sum_i V_i. \tag{21}$$

The second term represents dipole-like behaviour with the dipole strength given by

$$\boldsymbol{d}(t) = \int_S \left(\hat{\mathbf{n}}\varphi - \mathbf{x}\frac{\partial \varphi}{\partial n}\right)\mathrm{d}S. \tag{22}$$

It can be shown (see Lighthill [16]) that for a bubble in an infinite fluid, the dipole strength is related to the Kelvin impulse $\mathbf{I}$, by writing equation (22) as

$$\boldsymbol{d}(t) = \frac{\mathrm{d}}{\mathrm{d}t}(V\mathbf{x}_c) + \frac{1}{\rho}\mathbf{I}, \tag{23}$$

where $\mathbf{x}_c$ denotes the centroid position of the bubble configuration. In order to remove the source-like behaviour, and to preserve the individual bubble areas $V_1, \ldots, V_N$, the constraint equation

$$\oint_{S_i} \frac{\partial \varphi}{\partial n}\,\mathrm{d}S_i = 0, \quad i = 1, \ldots, N, \tag{24}$$

is applied to each surface.

To solve equation (18) together with equation (24) uniquely, and to calculate the unknown values p_i we now define a new potential on each surface given by,

$$\phi_i(\mathbf{x}) = \varphi(\mathbf{x}) + \lambda_i(t), \quad \mathbf{x} \in S_i, \tag{25}$$

where the pressure integral variable $\lambda_i(t)$ is given by

$$\lambda_i(t) = \int_0^t \Delta p_i(\tau)\,\mathrm{d}\tau. \tag{26}$$

By specifying the potential on each contour to within an unknown additive constant we therefore solve the problem as a modified Dirichlet problem (Muskhelishvili [17]). With this new potential, equation (14) now takes the form

$$\frac{D\phi_i}{Dt} = \frac{1}{2}|\mathbf{u}|^2 + \frac{4}{\mathrm{Eo}}\left(\kappa - \frac{1}{R_i}\right) + (\gamma_i - y), \tag{27}$$

and equation (18) becomes,

$$\frac{1}{2}(\phi_i(\mathbf{x}) - \lambda_i) = \sum_{I=1}^{N} \oint_{S_I} \left(G(\mathbf{x}, \mathbf{x}')\frac{\partial \varphi(\mathbf{x}')}{\partial n} - \{\phi_I(\mathbf{x}') - \lambda_I\}\frac{\partial G(\mathbf{x}, \mathbf{x}')}{\partial n'}\right)\mathrm{d}S_I'. \tag{28}$$

As $\mathbf{x} \in S_i$, the last integral is given by,

$$\oint_{S_I} \frac{\partial G(\mathbf{x}, \mathbf{x}')}{\partial n'} \, \mathrm{d}S_I' = \frac{1}{2\pi} \oint_{S_I} \frac{\partial \theta(\mathbf{x}, \mathbf{x}')}{\partial s'} \, \mathrm{d}S_I' = \frac{1}{2}, \tag{29}$$

where $\theta(\mathbf{x})$ is the angle between $\mathbf{x}$ and the x-axis.

The final form of the boundary integral formulation can now be written,

$$\frac{1}{2}\phi_i(\mathbf{x}) = \lambda_i + \sum_{I=1}^{N} \oint_{S_I} \left(G(\mathbf{x}, \mathbf{x}') \frac{\partial \varphi(\mathbf{x}')}{\partial n} - \phi_I(\mathbf{x}') \frac{\partial G(\mathbf{x}, \mathbf{x}')}{\partial n'} \right) \mathrm{d}S_I'. \tag{30}$$

3. Numerical implementation

3.1. Integration in Space

To represent the solution of the governing equations in discretised form, the bubble surfaces S_i, are divided into individual subintervals $S_{i,j}$, and a piecewise linear approximation is constructed. The subscript i $(= 1, \ldots, N)$ will again denote a particular bubble surface with j $(= 1, \ldots, M)$, designating a node point $\mathbf{x}_{i,j}$ on that surface, where M is the total number of nodes on each surface. The isoparametric representation used for the surfaces, potentials and normal derivatives, are of the form

$$\mathbf{x}(\xi) = \mathbf{x}_{i,j} F_1(\xi) + \mathbf{x}_{i,j+1} F_2(\xi), \tag{31}$$

$$\phi(\xi) = \phi_{i,j} F_1(\xi) + \phi_{i,j+1} F_2(\xi), \tag{32}$$

$$\mu(\xi) = \mu_{i,j} F_1(\xi) + \mu_{i,j+1} F_2(\xi). \tag{33}$$

where $\xi \in (0, 1)$ and

$$\left.\begin{aligned} F_1(\xi) &= 1 - \xi, \\ F_2(\xi) &= \xi, \end{aligned}\right\} \tag{34}$$

and μ is defined as $\partial\phi/\partial n$ with

$$\phi_{i,j} = \phi_i|_{\mathbf{x}_{i,j}} \quad \text{and} \quad \mu_{i,j} = \mu_i|_{\mathbf{x}_{i,j}}. \tag{35}$$

With this notation adopted, the discretized form of equations (24) and (29) yields a set of $N \times (M + 1)$ algebraic equations for the unknown values comprising, $N \times M$ normal derivatives and N constants λ_i

$$\frac{1}{2}\phi_{i,j} + \sum_{I=1}^{N} \sum_{J=1}^{M} \left(A_{I,J,1}^{i,j} \phi_{I,J} + A_{I,J,2}^{i,j} \phi_{I,J+1} \right) = \lambda_i + \sum_{I=1}^{N} \sum_{J=1}^{M} \left(B_{I,J,1}^{i,j} \mu_{I,J} + B_{I,J,2}^{i,j} \mu_{I,J+1} \right), \tag{36}$$

$$\sum_{J=1}^{M} \left(C_{I,J,1} \mu_{I,J} + C_{I,J,2} \mu_{I,J+1} \right) = 0, \quad I = 1, \ldots, N. \tag{37}$$

The coefficients $A^{i,j}_{I,J,L}$, $B^{i,j}_{I,J,L}$ and $C_{I,J,L}$ are evaluated from equations (30)–(36) as

$$A^{i,j}_{I,J,L} = \frac{1}{2\pi}\int_0^1 F_L(\xi)\frac{\partial}{\partial n_\xi}\left\{\log\frac{1}{|\mathbf{x}_{i,j}-\mathbf{x}'(\xi)|}\right\} d_{I,J}\,\mathrm{d}\xi, \tag{38}$$

$$B^{i,j}_{I,J,L} = \frac{1}{2\pi}\int_0^1 F_L(\xi)\left\{\log\frac{1}{|\mathbf{x}_{i,j}-\mathbf{x}'(\xi)|}\right\} d_{I,J}\,\mathrm{d}\xi, \tag{39}$$

and

$$C_{I,J,L} = \int_0^1 F_L(\xi)\, d_{I,J}\,\mathrm{d}\xi = \frac{1}{2}\, d_{I,J} \tag{40}$$

where $d_{I,J} = |\mathbf{x}_{I,J+1} - \mathbf{x}_{I,J}|$, is the segment length of $S_{I,J}$.

By expressing the above set of equations in the form

$$\frac{1}{2}\phi_{i,j} + \sum_{I=1}^{N}\sum_{J=1}^{M}\hat{H}^{i,j}_{I,J}\phi_{I,J} = \lambda_i + \sum_{I=1}^{N}\sum_{J=1}^{M}G^{i,j}_{I,J}\mu_{I,J}, \tag{41}$$

$$\sum_{J=1}^{M}G_{I,J}\mu_{I,J} = 0 \quad I = 1,\ldots,N, \tag{42}$$

and defining $H^{i,j}_{I,J} = \hat{H}^{i,j}_{I,J} + \delta_{i,I}\delta_{j,J}$, the above equation may be written down in matrix form as,

$$\mathbf{H}\phi = \mathbf{G}\mu. \tag{43}$$

This system can then be solved yielding the required values, $\mu_{i,j}$ at each node point.

In general the integrations described above are performed numerically using a 4-point Gauss rule. For the case when the collocation point $\mathbf{x}_{i,j}$ is within the segment $S_{I,J}$, or is one of its end points, in which case the integrand is singular, the integral must be treated specially. For these cases the $H^{i,j}_{I,J}$ and $G^{i,j}_{I,J}$ integrals are computed analytically.

3.2. Integration in time

The solution of equation (43) yields an approximation to $\partial\phi/\partial n$, prior knowledge of ϕ on S enables an approximation to $\partial\phi/\partial s$ at the collocation points. The velocity of the fluid particles $\mathbf{u}_{i,j}$ on the bubble surfaces can be evaluated using equation (3). Subsequently, the position of each surface is updated by employing a simple Euler scheme to all the node points,

$$\mathbf{x}^{(k+1)}_{i,j} = \mathbf{x}^{(k)}_{i,j} + \mathbf{u}^{(k)}_{i,j}\delta t^{(k)} + O\left[(\delta t^{(k)})^2\right], \quad k = 0, 1, 2, \ldots \tag{44}$$

where the superscript k denotes the time iteration. The same scheme is then applied to equation (27) to obtain the potential on this new surface as,

$$\phi^{(k+1)}_{i,j} = \phi^{(k)}_{i,j} + \left.\frac{D\phi}{Dt}\right|_{\mathbf{x}_{i,j}}\delta t^{(k)} + O\left[(\delta t^{(k)})^2\right]. \tag{45}$$

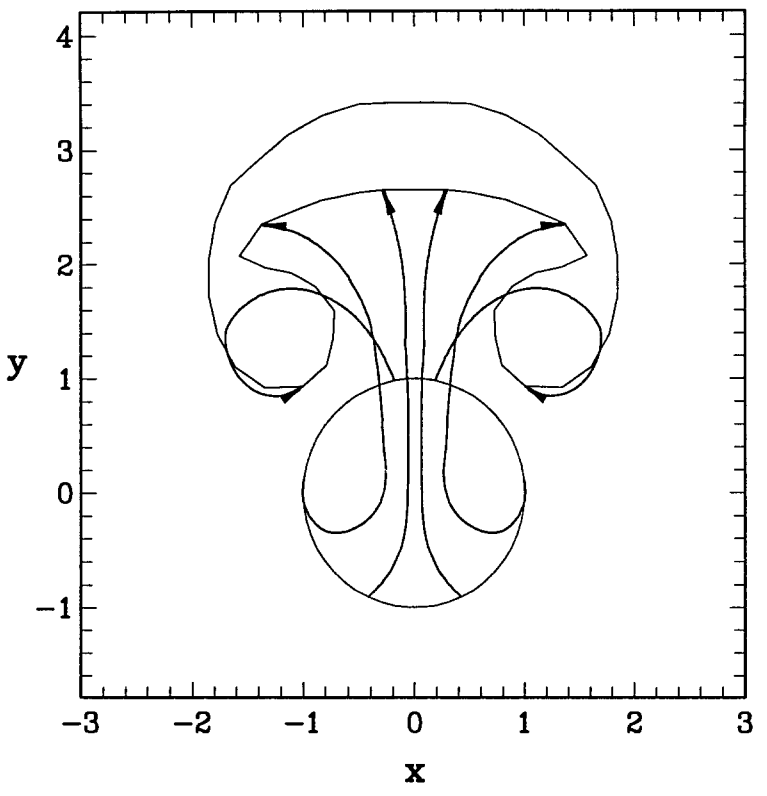

Fig. 2. The particle paths of six points lying on the bubble surface for the case of a single large bubble where surface tension effects are negligible. The trajectories indicate how points are "swept" into the jet formed at the rear.

In order to approximate the curvatures $\kappa_{i,j}$ given by

$$\kappa_{i,j} = \hat{\mathbf{n}} \cdot \left.\frac{\partial \mathbf{T}}{\partial s}\right|_{\mathbf{x}_{i,j}}, \tag{46}$$

the tangent $\mathbf{T}$ and the tangential velocity $\partial\phi/\partial s$ at the node points, a quadratic Lagrangian interpolation polynomial is used.

At each time step, $\delta t^{(k)}$ is chosen (see Blake *et al.* [18], Best and Kucera [19]) such that

$$\delta t^{(k)} = \min_{i,j} \left\{ \left| \left.\frac{\Delta\phi}{D\phi/Dt}\right|_{\mathbf{x}_{i,j}} \right| \right\}, \tag{47}$$

thereby restricting the maximum potential change at the bubble surface to $\Delta\phi$. This scheme possess the necessary features to enable the time integration technique to capture jet formation with δt reduced when the fluid motion is fast, and computational effort somewhat optimised.

The above procedure is repeated throughout the evolution of the bubble surfaces yielding the time history of the bubble shapes. To prevent the formation of uneven node densities along the surface (see Fig. 2), the collocation points are redistributed evenly over the bubble surface whenever

$$\frac{1}{2NM} \sum_{I=1}^{N} \sum_{J=1}^{M} d_{I,J} > \min_{i,j}\{d_{I,J}\}. \tag{48}$$

In order to approximately conserve the individual bubble area, quadratic interpolation is used to re-allocate the nodal positions and potentials. The bubble surface and potential is also smoothed periodically (see Blake *et al.* [18], Best and Kucera [19]) using the five-point smoothing formula of Longuet-Higgins and Cokelet [20] to help suppress the formation and subsequent amplification of surface oscillations introduced numerically through the temporal and spatial discretisation.

For a function f defined on an evenly spaced mesh, we chose a smoothed value $\bar{f}_{i,j}$ at $\mathbf{x}_{i,j}$ given by

$$\bar{f}_{i,j} = \frac{1}{16}(-f_{i,j-2} + 4f_{i,j-1} + 10f_{i,j} + 4f_{i,j+1} - f_{i,j+2}). \tag{49}$$

Smoothing is almost always required in problems of this type where the effect of surface tension is important [21]. Rapidly oscillating, small-scale capillary waves introduced mainly as a result of the surface discretisation can, if unchecked, be advected around the bubble surface towards the equator. Here the streamlines are closer and so the waves will have a longer wavelength and will be less easily stabilised by surface tension [22].

3.3. Streamlines and Pressure Contours

To fully understand the basic physics of bubble interaction, consideration needs to be given to the ambient flow and pressure fields which induce the bubble motion.

By exploiting the complex potential Φ defined for $\mathbf{x} \in \Omega^-$ by

$$\Phi = \phi(\mathbf{x}) + i\psi(\mathbf{x}), \tag{50}$$

the stream function $\psi(\mathbf{x})$ is given as the conjugate harmonic function to (28) by

$$\psi(\mathbf{x}) = \int_S \left(-\theta(\mathbf{x}' - \mathbf{x}) \frac{\partial \varphi(\mathbf{x}')}{\partial n} - \phi(\mathbf{x}') \frac{\partial G(\mathbf{x}, \mathbf{x}')}{\partial s'} \right) \mathrm{d}S', \quad \mathbf{x} \in \Omega^-. \tag{51}$$

The multivalued angle between the vector $\mathbf{x}' - \mathbf{x}$ and the x-axis is given by the function $\theta(\mathbf{x}' - \mathbf{x})$ described in Jaswon and Symm [23] which, for a fixed point $\mathbf{x}$, is continuous as $\mathbf{x}'$ describes any bubble surface.

The pressure at a point $\mathbf{x}$ in the fluid is given by the Bernoulli condition of equation (4),

$$p(\mathbf{x}) = 1 - \frac{1}{2}(\nabla\varphi)^2 - \frac{\partial \varphi}{\partial t} - y, \tag{52}$$

where the potential φ is given by equations (25) and (29) by

$$\varphi(\mathbf{x}) = \sum_{I=1}^{N} \oint_{S_I} \left(G \frac{\partial \varphi(\mathbf{x}')}{\partial n} - \phi_I \frac{\partial G}{\partial n'} \right) \mathrm{d}S'_I, \quad \mathbf{x} \in \Omega^-. \tag{53}$$

The derivatives of the potential in the fluid are calculated by finite difference methods.

4. Computational Results

In this section we present a selection of examples obtained using the boundary integral method as described in the previous sections. Since for each calculation the number of bubbles, the initial bubble positions, the Eötvös number and the relative bubble areas are all chosen

freely, the results given do not give a completely exhaustive description of the many and varied bubble interactions to be found. Instead, in an attempt to understand the underlying fundamental dynamics of the interactions, we limit the number of bubbles in the configuration to at most three and consider the effect of bubbles rising side-by-side and above one another. In addition we examine the behaviour of a pair of small bubbles for various angles between the line-of-centres and the direction of the gravity vector with a view to determining the effect of bubble deformation. In all the calculations, the number of nodes on each bubble surface was $M = 60$ and the maximum potential change at the bubble surface was taken as $\Delta\phi = 0.05$. The calculations were performed on a Sun Microsystems Sparcstation 10, model 30 with a typical – at least for the larger bubbles where considerable jetting and surface self-intersection occurs forcing calculations to stop – computational time of approximately 2 minutes, comprising about 170 time integration steps.

For a large bubble rising under the influence of gravity, the surface distorts and collocation points are "swept" around it, often into a jet formed at its rear. This effect is clearly demonstrated by the single bubble calculation of Fig. 2, where all of the material particles that are followed (including those located initially near the top of the surface) migrate into the jet. The node redistribution and smoothing scheme described in Section 3.2 is thus required to re-allocate node positions, so as to retain resolution at the tops of bubble surfaces and to help to prevent the occurrence of numerical instabilities.

In Fig. 3, the computed bubble shapes and centroid displacements are given for a vertical array of three equally sized circular bubbles with initial centroid separation of three radii. In this case Eo = 53, corresponding to relatively large bubbles of equivalent radii of 1 cm, so that surface tension effects are very small. At time $t = 1.26$, the formation of a jet at the rear of each bubble is apparent. As the bubbles continue to accelerate, mutual differences in deformation are clearly visible. As each bubble rises, fluid is displaced around its surface, the overall shape of which is largely governed by the speed of this flow. The leading bubble, which rises into relatively undisturbed fluid, develops a wide profile, while the lower bubbles, able to slip-stream the upper bubble, develop narrower profiles and so accelerate faster, as the shapes develop. This can be seen in the final frame of Fig. 3. By time $t = 2$ the top, middle and lower bubble centroids have moved 1.6, 1.9 and 1.6 radii respectively, but the lower bubbles subsequently accelerate and the top bubble slows down due to the significant shape changes occurring around this time.

Lower virtual masses as a result of the narrower bubble shapes of the lower two bubbles is not the sole reason for their greater centroid velocities. In fact the centroid of the central bubble rises fastest as a consequence of the bubble being drawn up with the fluid into the wider jet of the upper bubble; this feature of interaction is less pronounced between the lower two bubbles.

As the liquid jets continue to develop, the elongation of the lower bubbles mentioned above becomes quite considerable. Indeed, at $t = 2.5$ the trailing bubble is approximately twice as tall and half as wide as the leading bubble. In both of the lower bubbles the jet evolves into an anvil shape in a similar manner to that of a single bubble, leading to necking of the surface and the formation of two lobes. In the leading bubble, the jet takes on a much broader shape due to the entrainment of the second bubble, and necking does not occur.

In Fig. 4a, the pressure contours for the configuration corresponding to Fig. 3 are given at time $t = 1.9$. Towards the outer edges of the frame, where the fluid is relatively undisturbed, the hydrostatic pressure inducing the bubble rise can be seen. Adjacent to each bubble, regions of lower pressure are formed where the flow over the surfaces is faster. Directly below each

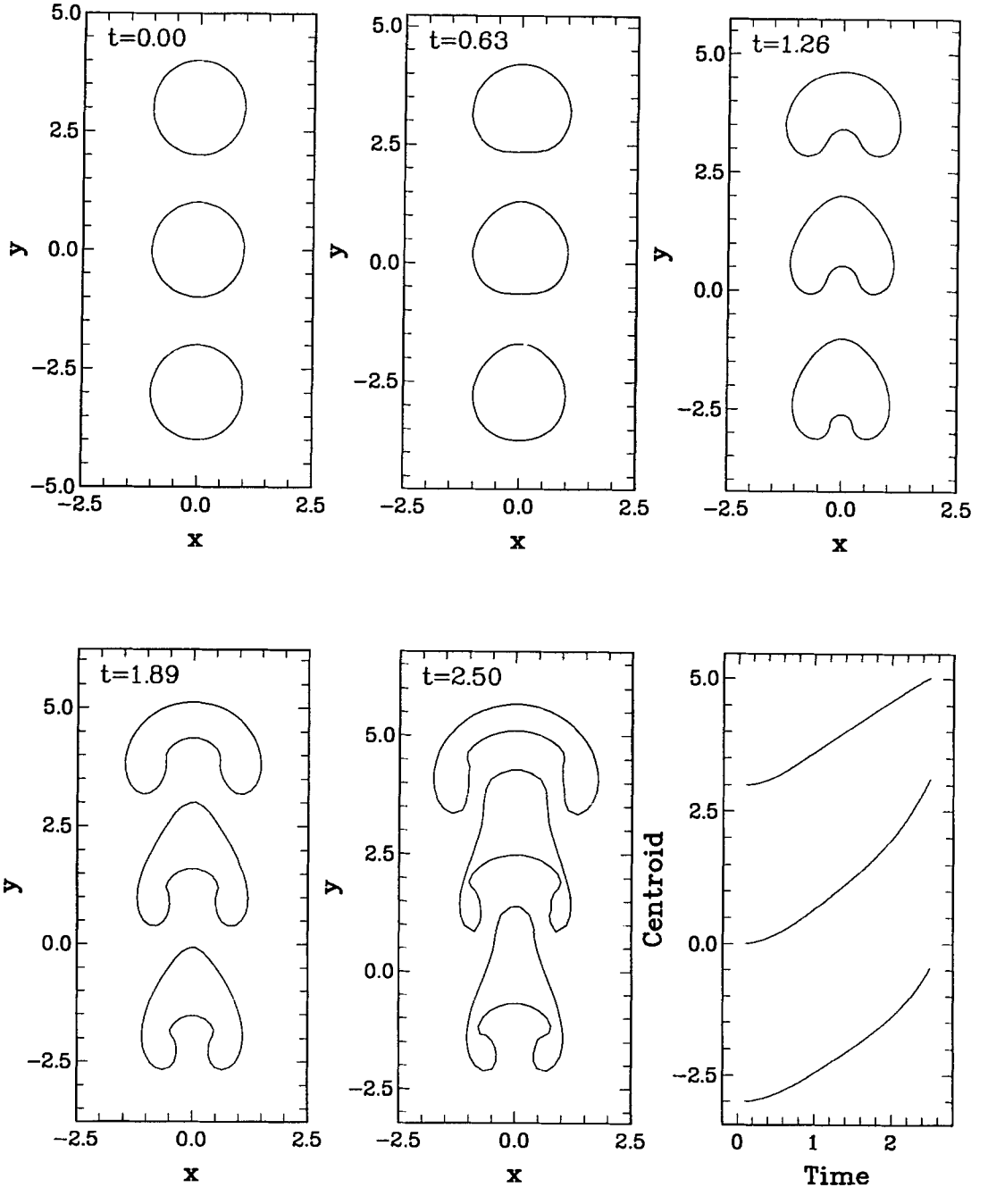

Fig. 3. The evolution of bubble shape and centroid positions for a configuration of three equally sized bubbles rising beneath each other. The parameters are given by Eo = 53, $\gamma_1 = 3$, $\gamma_2 = 0$, $\gamma_3 = -3$ and $\delta_1 = \delta_2 = \delta_3 = 0$.

bubble, regions of higher pressure are visible which are responsible for the production of the liquid jets. In Fig. 4b the corresponding streamlines for the configuration at $t = 1.9$ are shown. As predicted by equation (22), the overall behaviour is essentially that of a dipole. The two closest bubbles of the system being the upper two bubbles also "pair off" exhibiting strong dipole behaviour. The increased fluid velocities associated with the increased density

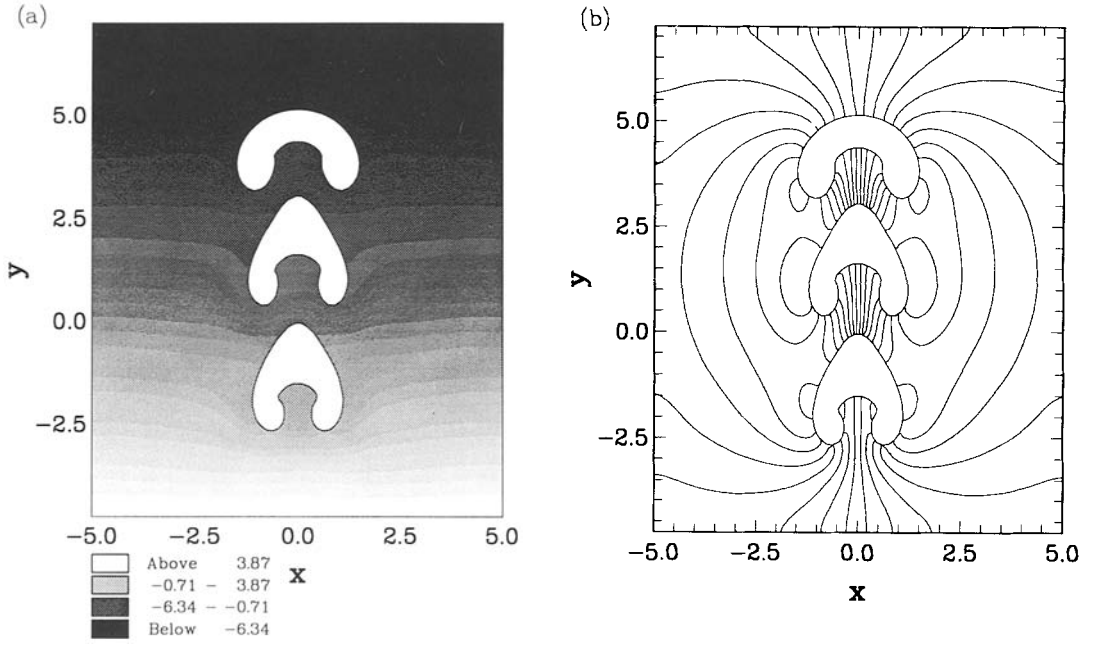

Fig. 4. Pressure contours (a) and streamlines (b) plotted for the system in Fig. 3 at a dimensionless time $t = 1.9$.

of streamlines into the jets is also evident. The other feature of note is the "trapping" of fluid between the bubbles as evidence by the near parallel streamlines.

In Fig. 5, the computed bubble shapes and centroid displacements are given for a horizontal array of two bubbles of equal size with an initial centroid separation of three equivalent radii. As in the previous case, the Eötvös number is given by Eo = 53, corresponding to bubbles of equivalent radii of 1 cm. Due to the symmetry of the problem about the y-axis, there is no flow across this line. In this geometry the two bubble system is equivalent to the problem of a single bubble rising in an ideal fluid along-side a vertical wall defined by the line $x = 0$, with the other bubble acting as its image.

At time $t = 1.32$, the formation of a jet at the trailing edge of each bubble is clearly evident. As in the case of cavitation bubble collapse near a rigid boundary, the fluid on the outer sides of the configuration has greater mobility than that of the more restricted flow close to the line of symmetry where the horizontal component of the velocity must be almost zero. Since the liquid jets comprise essentially of fluid which has circulated around the outside of the configuration, the inertia in the fluid dictates that they therefore develop such that they are directed at an angle towards the line of symmetry. By about $t = 2.6$ the jets have broadened, again by developing the characteristic anvil shape which subsequently impinges upon the inner sides of each bubble.

Reference to the final frame of Fig. 5 indicates that by time $t = 2$ the bubble centroids have risen just 1.0 radius as opposed to over 1.5 times this for the case of the vertical arrangement depicted in the previous figures. This is mainly due to the slip-steaming nature of the flow in the vertical case lowering the effective virtual mass of each of the bubbles there.

In Fig. 6a, the pressure contours for the configuration of Fig. 5 are given at time $t = 1.9$. The high pressure region responsible for the production of the liquid jet is evident in the lower portion of the figure, along with a further high pressure region associated with the stagnation

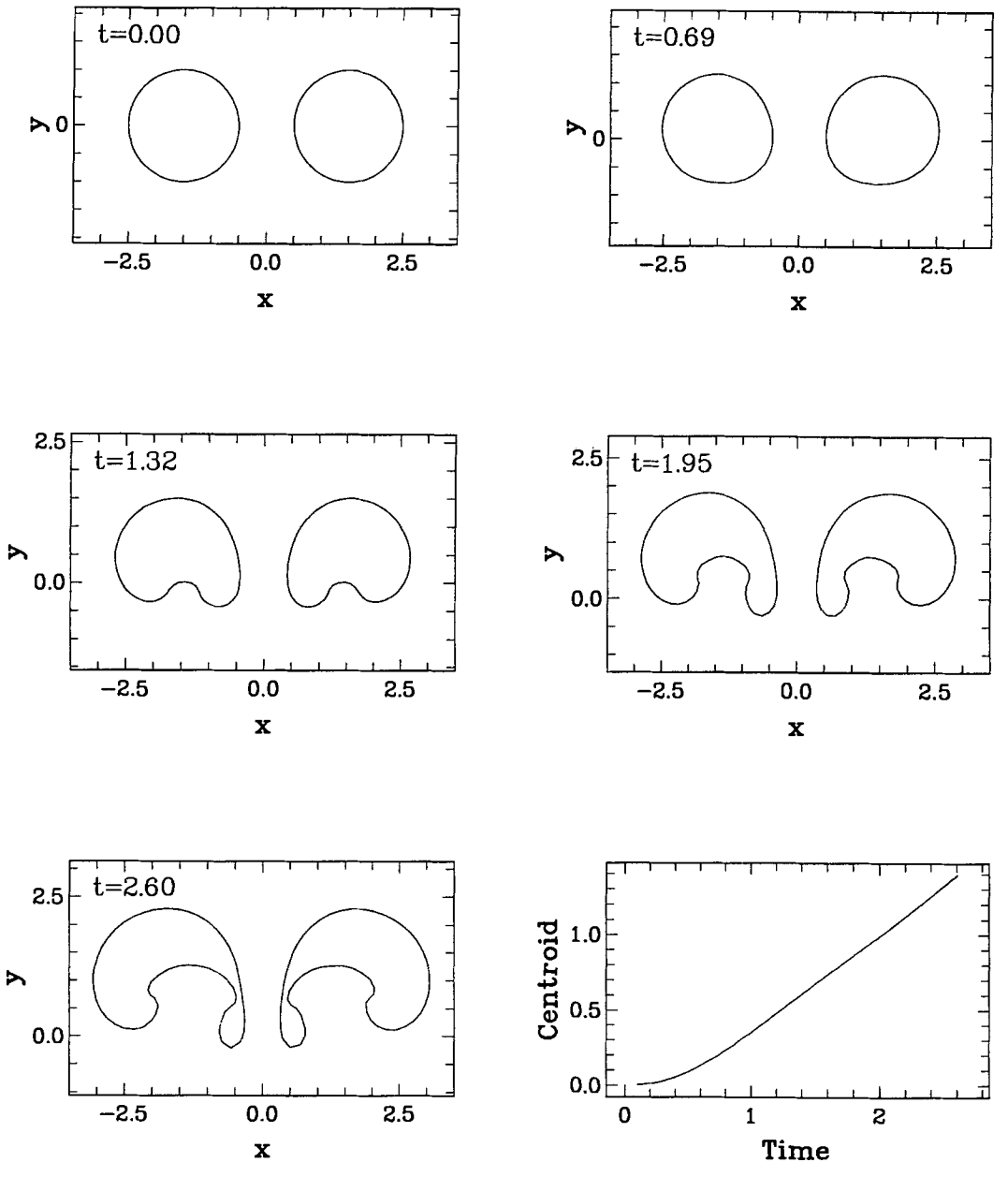

Fig. 5. The evolution of bubble shape and centroid positions for a configuration of two equally sized bubbles rising side-by-side. Here Eo = 53, $\gamma_1 = \gamma_2 = 0$, $\delta_1 = 1.5$ and $\delta_2 = -1.5$.

point generated on the line of symmetry. In Fig. 6b, the corresponding streamlines again indicate that the surrounding flow field exhibits essentially dipole behaviour. In the vicinity of the jets, a prominent increase of streamline density generated by increased fluid velocities can be seen. The majority of these streamlines can be observed to circulate from the outer sides of the configuration thus producing the slanted jets.

In Fig. 7, the computed bubble shapes are given for an array of two equally sized bubbles at intervals of 1.0 from $t = 0$ to $t = 5$. In this case, the Eötvös number is given by Eo = 0.53 corresponding to relatively small bubbles of radii 1 mm. For such small bubbles, the effect of

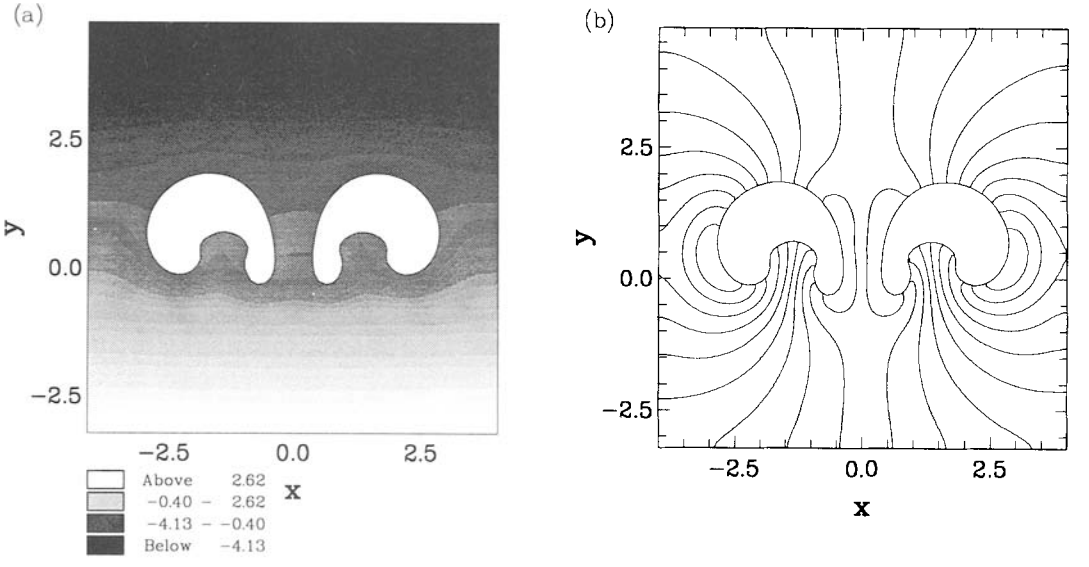

Fig. 6. Pressure contours (a) and streamlines (b) plotted for the system in Fig. 5 at a dimensionless time $t = 1.9$.

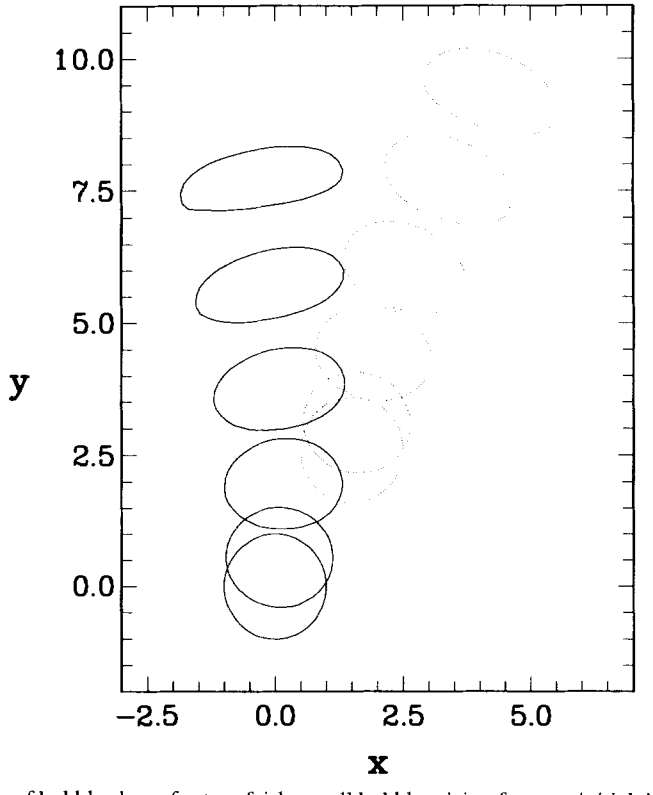

Fig. 7. The evolution of bubble shape for two fairly small bubbles rising from an initial diagonal displacement. In this case the Eötvös number is given by Eo = 0.53 with $r = 3$ and $\theta = 30°$.

surface tension is significant and no jet formation occurs on the bubble rear surfaces. However, the increased velocity of fluid flow past the sides of the bubbles, results in the formation of local low pressure regions. Consequently, by time $t = 3$ they have started to flatten. The slightly higher pressure in the slower moving fluid between the bubbles forces the upper bubble to flatten so that its longer axis points almost in the direction of its relative motion with respect to the lower bubble. This effect was mentioned in Duineveld [10] (p. 50) and is essentially a consequence of the fact that the upper bubble motion is disturbed slightly from the vertical, the direction of movement being perpendicular to the direction of the longer axis. The fact that the lower bubble seems to rise almost vertically with only a slight drift to the left is verified by the small inclination of this bubble in that direction; the upper one moves sideways, to the right, more rapidly and is inclined at a greater angle.

In order to determine the possible consequences of the deformation, in Fig. 8(a) we plot the relative trajectory of the centroid of the upper bubble (bubble 2) with respect to that of the lower bubble (bubble 1) for angles between the vertical and the line-of-centres (see Fig. 1) of $\theta = 15°, 30°, 60°$ and $80°$, with an initial separation of $r = 3$. In Fig. 8(b) the change in height of the centroid of the bubble system pair is plotted against time. We compare this, in Figs. 9(a) and (b), against the case when Eo = 0.13 (0.5 mm) where bubble deformation is lower, corresponding more closely to the calculations of Kok [8], albeit in only two dimensions. The shortness of the trajectories for the $\theta = 60°$ and $\theta = 80°$ cases is a result of collisions between the bubbles at an early stage in the rise causing the calculations to halt.

The difference between figures 8 and 9 is significant. For $\theta > 15°$ (see Figs. 8(a) and 9(a)) the upper bubble of the larger, more deformable pair moves downwards, around the lower bubble more slowly. This shallower slope for the trajectories of the large-bubble cases may be due to the fact that the virtual masses of these bubbles are least when moving in an almost horizontal direction, corresponding to the direction perpendicular to their shorter axes. Thus if we assume other hydrodynamic effects of the flow-field due to a small deformation to be negligible, we expect, for a given force, the resultant motion of the upper bubbles to be faster in the cross-stream direction than in the stream-wise direction. The greater upward acceleration of the $\theta = 15°$ case for the smaller bubble may be explained in the same way.

Inspection of Figs. 8(b) and 9(b) shows that, although the vertical motion of each of the corresponding bubble systems is initially identical in both cases, as the bubbles of Fig. 8 start to deform, their velocity becomes almost constant whereas those in Fig. 9 continue to accelerate at a steady rate, thereby rising about 1.5 times further by time $t = 6.5$. This is again due to the increase in virtual mass as a result of the deformation of the bubbles in Fig. 8, with the consequence that the time-scales for the corresponding trajectories of Figs. 8(a) and 9(a) differ considerably, particularly for the cases $\theta = 15°$ and $30°$, where no collision occurs here for smaller angles, with these bubble-pairs rising faster.

Unfortunately, the effect apparent in Figs. 8(a) and 9(a) does not seem to explain the slight differences between the experimental and calculated plots in Kok's [9] figure 9, where the trajectories for the deformable experimental bubbles are steeper than for the spherical bubbles predicted by the theory. Also, while the difference in the time-scale seen here may appear to explain why Kok's predicted relative bubble motion is too rapid, he asserts that their absolute rise velocity agrees well with experiment. Thus, without additional numerical calculations which include further physical phenomena, such as viscous drag and rotational wake formation, it is difficult to quantify other interaction effects which occur as a result of bubble deformation and hence explain fully the experimental results as reported by Kok [9]. Indeed, it is interesting to note that the effect of deformation has already been shown to be

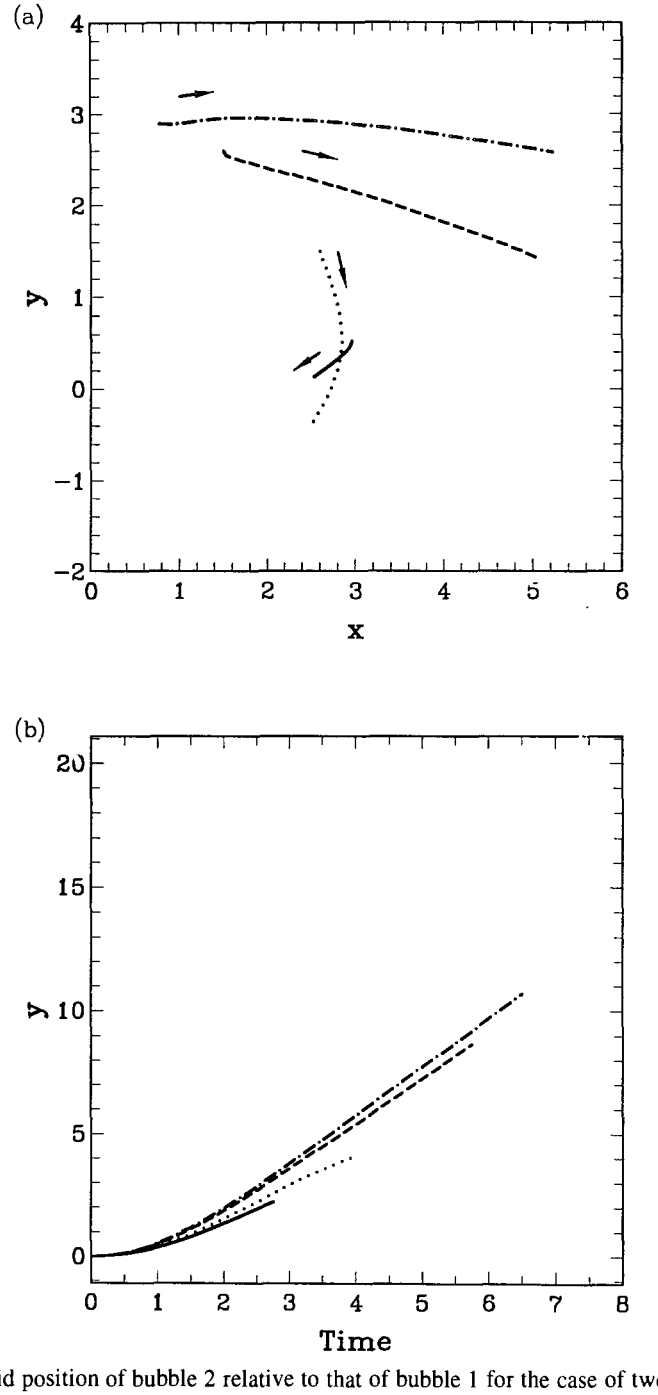

Fig. 8. (a) The centroid position of bubble 2 relative to that of bubble 1 for the case of two fairly small bubbles (Eo = 0.53) rising from an initially diagonal displacement given by $r = 3$ and $\theta = 15°$ (— · —), 30° (— — —), 60° (· · ·) and 80° (—). The direction of motion is indicated by arrows. (b) The height of each bubble pair system, plotted against time.

of great significance in the study of bubbles rising in shear flows (for a numerical study see Esmaeeli *et al.* [24]). Here, for both the two and three-dimensional cases, the sense of the

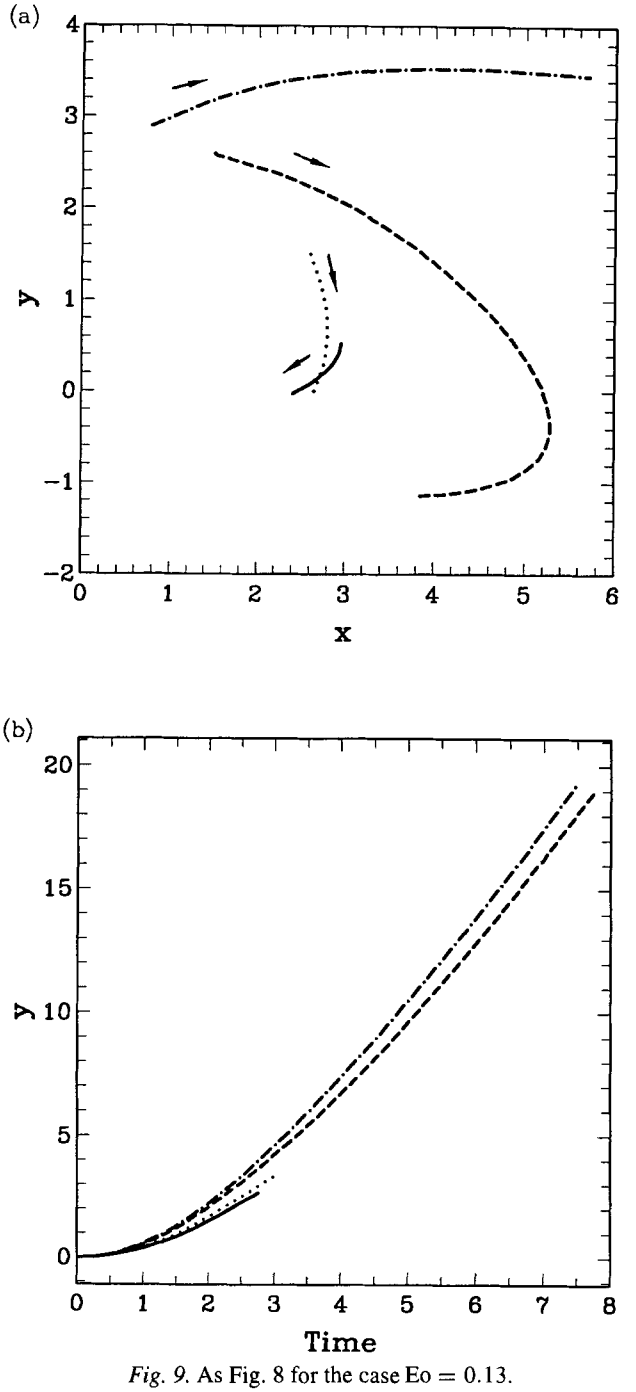

Fig. 9. As Fig. 8 for the case Eo = 0.13.

resultant circulation around the bubble and hence the direction of the lift force induced for deformable bubbles is opposite to that for the corresponding undeformable bubbles.

5. Conclusions

This study is a numerical extension to the classic work by Walters and Davidson [1] to a multi-bubble two-dimensional configuration. It provides a valuable insight into fully three-dimensional behaviour which will require much more extensive and detailed computation. Buoyancy and surface tension effects are also included in these calculations.

The key feature of the single bubble studies is often the formation of a broad-based jet that spreads out ultimately splitting off two bubbles. If symmetry is maintained with a line of bubbles, "shedding" and "trapping" of fluid between the bubbles occurs. For three identical, equally-spaced bubbles, the upper two break away from the lower one, owing to the middle bubble's greater velocity. Eventually these bubbles, beginning with the middle one, shed two bubbles as in the single bubble case.

When the symmetry is broken by the addition of further bubbles, the bubbles and jets formed become skewed and the shedding of smaller bubbles no longer occurs in simultaneous pairs. Stagnation flow can also develop above pairs of bubbles.

By considering the interaction of a pair of small bubbles, rising from different initial configurations, we have been able to indicate a significant effect of bubble deformation on the relative motion of the bubbles.

The numerical implementation developed in this paper may be employed for a finite number of bubbles up to the limitations of the available computing power. For example, it could easily be extended to consider the multiple arrival of bubbles at a free surface as is so important in chemical engineering and bio-reactor studies. The single bubble studies of this for the two-dimensional case have been presented in Boulton-Stone [25] and the bursting of an axisymmetric bubble at a free surface by Boulton-Stone and Blake [26]. Finally it should be re-iterated that the boundary integral method is an excellent numerical tool for modelling the time-dependent initial motion associated with mutually interacting bubbles.

References

1. J.K. Walter and J.F. Davidson, The initial motion of a gas bubble in an inviscid liquid. Part I. The two-dimensional bubble. *J. Fluid Mech.* 12 (1962) pp. 408–417.
2. R.T. Baumel, S.K. Burley, D.F. Freeman, J.K. Gammel and J. Nuttall, The rise of a cylindrical bubble in an inviscid liquid. *Can J. Phys.* 60 (1982) pp. 997–1007.
3. G.R. Baker and D.W. Moore, The rise and distortion of a two-dimensional bubble in an inviscid liquid. *Phys. Fluids A*, 1(9) (1989) 1451–1459.
4. J.R. Blake, P.B. Robinson, A. Shima and Y. Tomita, Interaction of two cavitation bubbles with a rigid boundary. *J. Fluid Mech.* 255 (1993) 707–721.
5. S.O. Unverdi and G. Tryggvason, A front-tracking method for viscous, incompressible, multifluid flows. *J. Comp. Phys.* 100(1) (1992) 25–37.
6. R. Clift, T.J.R. Grace and M.E. Weber, *Bubbles, Drops, and Particles*. Academic Press, 1978.
7. D. Bhaga and M.E. Weber, Bubbles in viscous liquids: shapes, wakes and velocities. *J. Fluid Mech.* 105 (1981) 61–85.
8. J.W.B. Kok, Dynamics of a pair of gas bubbles moving through fluid. Part I. Theory. *European J. Mechanics B/Fluids*, 12(4) (1993) 525–540.
9. J.W.B. Kok, Dynamics of a pair of gas bubbles moving through fluid. Part II. Experiment. *European J. Mechanics B/Fluids*, 12(4) (1993) 541–560.
10. P.C. Duineveld, *Bouncing and coalescence of two bubbles in water*. PhD thesis, The Netherlands, Twente University, (1994).
11. V. Kumaran and D.L. Koch. The rate of coalescence in a suspension of high Reynolds number, low Weber number bubbles. *Phys. Fluids* 5 (1993) 1135–1140.
12. L. van Wijngaarden. The mean rise velocity of pairwise interacting bubbles in liquid. *J. Fluid Mech.* 251 (1993) 55–78.

13. M. Manga and H.A. Stone, Buoyancy-driven interactions between two deformable viscous drops. *J. Fluid Mech.* 256 (1993) 647–683.
14. J.F. Harper, The motion of bubbles and drops through liquids. *Adv. Appl. Mech.* 12 (1972) 59–129.
15. G.K. Batchelor, *An Introduction to Fluid Dynamics*, Cambridge University Press, 1967.
16. M.J. Lighthill, *An informal Introduction to Fluid Mechanics*, Oxford University Press, 1986.
17. N.I. Muskhelishvili, *Singular Integral Equations*, Noordhoff, (1953).
18. J.R. Blake, B.B. Taib and G. Doherty, Transient cavities near boundaries. Part II. Free surface. *J. Fluid Mech.* 181 (1987) 197–212.
19. J.P. Best and A. Kucera, A numerical investigation of nonspherical rebounding bubbles. *J. Fluid Mech.* 245 (1992) 137–154.
20. M.S. Longuet-Higgins, On the forming of sharp corners at a free surface. *Proc. Roy. Soc. Lonc. A* 371 (1980) 453–478.
21. H.N. Oğuz and A. Prosperetti, Surface tension effects in the contact of liquid surfaces. *J. Fluid Mech.* 203 (1989) 149–171.
22. G.K. Batchelor, The stability of a large gas bubble rising through liquid. *J. Fluid Mech.* 184 (1987) 399–422.
23. M.A. Jaswon and G.T. Symm, *Integral Equation Methods in Potential Theory and Elastostatics*. Academic Press (1977).
24. A. Esmaeeli, E. Ervin and G. Tryggsvason, Numerical simulations of rising bubbles. In J.R. Blake, J.M. Boulton-Stone and N.H. Thomas, editors, *Bubble dynamics and interface phenomena*, Kluwer (1994).
25. J.M. Boulton-Stone, A comparison of boundary integral methods for studying the motion of a two-dimensional bubble in an infinite fluid. *Comp. Meths. in Appl. Mech. and Engng.* 102 (1993) 213–234.
26. J.M. Boulton-Stone and J.R. Blake, Gas bubbles bursting at a free surface. *J. Fluid Mech.* 254 (1993) 437–466.